Commun. Comput. Phys.
doi: 10.4208/cicp.OA-2024-0212

Vol. **39**, No. 5, pp. 1536-1558
May 2026

Multiscale Simulation of Rarefied Gas Flows in Simplified Divertor Tokamak Test Facility Particle Exhaust

Wei Li, Yanbing Zhang, Jianan Zeng and Lei Wu*

Department of Mechanics and Aerospace Engineering, Southern University of Science and Technology, Shenzhen 518055, China.

Received 4 September 2024; Accepted (in revised version) 22 December 2024

Abstract. Simulating gas flow within the divertor, which is a crucial component in nuclear fusion reactors, is essential for assessing and enhancing its design and performance. Traditional methods, such as the direct simulation Monte Carlo and the discrete velocity method, often fall short in efficiency for these simulations. In this study, we utilize the general synthetic iterative scheme to simulate a simplified Tokamak divertor model, demonstrating its fast convergence and asymptotic-preserving properties in complex three-dimensional scenarios. A conservative estimate of speedup by three orders of magnitude is achieved by the general synthetic iterative scheme when compared to the direct simulation Monte Carlo method. We further investigate the relationship between pumping efficiency and factors like temperature, absorptivity, and the Knudsen number, providing valuable insights to guide the design and optimization of divertor structures.

AMS subject classifications: 65-XX, 76-XX

Key words: Vacuum pump, rarefied gas flow, general synthetic iterative scheme.

1 Introduction

Nuclear fusion, a reaction process with immense energy potential, is considered a promising source of future clean energy. Divertors are essential components in fusion reactors, which enhance the efficiency and sustainability of fusion reactions by reducing energy loss and impurity accumulation. For example, the Divertor Tokamak Test (DTT) facility in Europe aims to conduct scaled experiments to develop divertor solutions compatible with the anticipated physical conditions and technological environment of the

*Corresponding author. *Email addresses:* wul@sustech.edu.cn (L. Wu), 12332503@mail.sustech.edu.cn (W. Li), 12132428@mail.sustech.edu.cn (Y. Zhang), 12031255@mail.sustech.edu.cn (J. Zeng)

DEMO reactor. The pumping rate is one of the critical factors in the design of divertor [1–3], and numerical methods are used to determine optimal pumping port configurations [4, 5]. However, the complex structure of divertor results in a wide range of Knudsen numbers (Kn, the ratio of mean molecular free path λ to the characteristic flow length L), and poses significant challenges in the numerical simulations, as the gas flow should be described by the Boltzmann equation rather than the traditional Navier-Stokes equations.

The Boltzmann equation can be solved by the stochastic direct simulation Monte Carlo (DSMC) method [6] and deterministic discrete velocity method (DVM) [7]. The DSMC uses simulation particles to mimic the streaming and collision of real gas molecules, and there are only a few simulation particles in each spatial cell. Therefore, it has become the prevailing method to simulate the rarefied gas dynamics as the usage of computer memory is acceptable. However, because the streaming and collision are splitted, the cell size and time step must be smaller than the mean free path and mean collision time of gas molecules, respectively, rendering the DSMC extremely time-consuming in simulating near-continuum flows. In order to improve the computational efficiency in the near continuous flow region, the NS-DSMC coupling method [8, 9] has been proposed, that is, the NS equation and DSMC method are used in the near continuous and rarefied flow regimes, respectively. However, in many engineering applications, it is difficult to distinguish the boundary between them. In order to avoid such problems, scholars have proposed a series of new methods such as the time relaxation Monte Carlo method [10, 11], the exponential Runge-Kutta method [12] and the asymptotic-preserving Monte Carlo method [13]. In addition, scholars have also conducted in-depth studies on stochastic methods. Fei *et al.* used the Chapman-Enskog expansion to eliminate first-order numerical flux errors and proposed a unified random particle Bhatnagar–Gross–Krook (BGK) method [14]; Pfeiffer *et al.* introduced the exponential differencing BGK method, which applies implicit integration to the BGK equation [15]. Kim *et al.* proposed a random particle Fokker-Planck method, which combined with stochastic interpolation technology and achieve second-order accuracy under fixed CFL conditions [16]. However, since the statistical averaging is needed, the DSMC is slow in resolving small and/or transit flow fields. As a consequence, in the simulation of DTT particle exhaust [1], 40 million spatial cells and 0.688 million CPU core hours are required to find the steady state, making the optimization of divertor difficult.

In DVM, in addition to the spatial discretization, the molecular velocity space is also discretized [17,18]. Since each physical cell contains thousands of discrete velocity points, the computer memory requirement can be hundreds times greater than that of the DSMC. However, due to its deterministic nature, the statistic averaging process is eliminated, making it faster than the DSMC in simulating low-speed and/or transit flows.

Early versions of DVM also separate the streaming and collision processes, leading to large numerical dissipation similar to the DSMC. In the past decades, significant progresses are made by Chinese scholars to eliminate these deficiencies and boost the simulation efficiency by several orders of magnitude. For example, the implicit unified gas-

kinetic scheme (UGKS) [19], the discrete unified gas kinetic scheme (DUGKS) [20], and the generalized synthetic iteration scheme (GSIS) [21–23] have been proposed and applied to challenging multiscale engineering applications. In UGKS and DUGKS, the analytic solution of the kinetic equation is utilized to simultaneously handle streaming and collision, and the limitation of spatial cell size is removed. In GSIS, the traditional DVM is used to solve the kinetic equations, together with the macroscopic synthetic equations to empower the fast convergence and asymptotic-preserving characteristics. As a consequence, steady-state solutions can be obtained within dozens of iterations across the entire range of gas rarefaction. Compared to the UGKS and its variants [20, 24], the flux evaluation in GSIS is much simpler, and more importantly, the macroscopic synthetic equations are solved to the steady state (while that in UGKS is only solved for one-time step), which significantly enhance the exchange of fluid information in the whole computational domain. As a result, if the same numbers of spatial cell and discrete velocity are used, the GSIS is faster [25]. For example, Tantos *et al.* have simulated two-dimensional simplified DEMO using DVM [26], although the method is faster than DSMC, it is much slower than the GSIS [23].

The aim of the present work is twofold. First, to use the GSIS to show that rarefied gas flows in divertor can be efficiently simulated. Second, to perform numerical simulations over a wide range of Knudsen number, temperature, and surface absorptivity to test the performance of the divertor.

The rest of the paper is structured as follows: Section 2 introduces the divertor geometry and flow configuration. Section 3 details the kinetic model and numerical method used. Section 4 validates the convergence of both spatial and velocity space discretizations. Section 5 systematically analyzes the impact of Knudsen number, absorptivity, and temperature on pumping speed. Finally, conclusions are presented in Section 6.

2 Statement of the problem

The computational paradigm employs the latest DTT divertor [5], simulating 20° toroidal sector in Fig. 1(a), out of the 18 sectors in total that form the entire DTT divertor ring. The origin model incorporates the inner surface of the vacuum vessel, the pumping duct, the poloidal gap, the toroidal interstice between the target and the divertor, as well as the toroidal magnetic coils and coolant conduits integrated within the divertor assembly. In this paper, we consider a simplified version of the divertor in Figs. 1(b) and 1(c), without considering the magnetic coils, the cooling pipes and the toroidal/poloidal gaps.

Neutral deuterium gas enters the simulation domain through the inner and outer entry gaps in Fig. 1(b). These inlets are modeled as surfaces with specific capture coefficients [1], that is, approximately 35% and 65% of the deuterium gas enters through the inner and outer entry gap, respectively. The flux of deuterium entering the divertor can

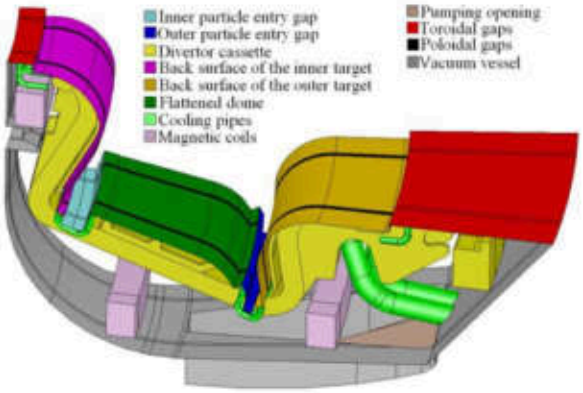

(a) Origin geometry

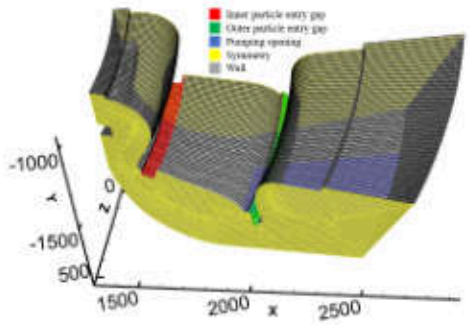

(b) Top view

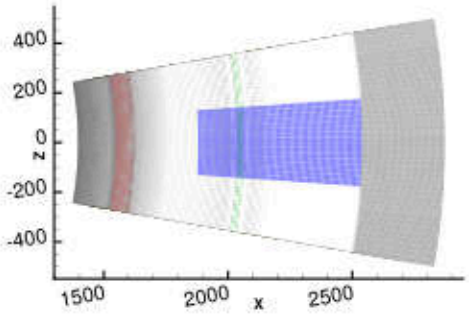

(c) Bottom view

Figure 1: (a) Original geometry of the divertor obtained from Ref. [1]. (b,c) The top and bottom views of the simplified geometry (dimensions in mm).

be expressed as:

$$\Phi_{in} = \frac{A}{4}\frac{\rho}{m}\sqrt{\frac{8k_BT}{\pi m}}, \tag{2.1}$$

where A is the area of the inner and the outer entry gap, k_B is the Boltzmann constant; ρ, m, and T are the density, molecular mass, and temperature of the gas, respectively. In typical operations, it is estimated in Ref. [1] that the number densities at the inner entry gap is 1×10^{21} m^{-3} and outer entry gap is 1.857×10^{21} m^{-3}.

The gas undergoes both inter-molecular collisions and interactions with the internal walls. Upon impacting with the walls, gas particles are reflected diffusely, where the wall temperature is maintained at 293 K. When gas molecules encounter the two lateral boundaries in Fig. 1(b), they undergo specular reflection back into the simulation domain to mimic the toroidal symmetry [27].

Beneath the divertor lies an absorption pump, which is located in the middle of the bottom of the divertor, see the blue area in Figs. 1(b) and 1(c). Gas molecules have a probability of being absorbed, with a specified pump probability ζ. That is, gas particles impinging on this surface have a probability ζ of being absorbed and a probability $1-\zeta$ of being diffusely reflected back into the divertor region. In the DTT, it is estimated that the pump probability ranges from $0.05 \leq \zeta \leq 0.3$.

In the design of the divertor, the efficacy of the absorption pump can be effectively gauged through the evaluation of parameters such as mass flow rate and pumping speed. From Eq. (2.1), we know that the inlet flux is determined by number density and temperature, while the outlet flux is primarily influenced by the outlet absorptivity. For a given set of density, temperature, and absorptivity ζ, the mass flow rate and pumping speed of the divertor are uniquely determined. This paper delves into the interplay between the Knudsen number, temperature, absorptivity, and the consequential impact on the mass flow rate of the absorption pump. By unraveling these relationships, valuable insights are gleaned to enhance the deflector's design and operational efficiency.

3 Numerical method

In this section, the gas kinetic model, the velocity discretization, the gas-surface boundary condition, and the GSIS, are introduced.

3.1 The kinetic model

Kinetic model equations simplified from the Wang-Chang & Uhlenbeck equation [28] are usually adopted in numerical simulations to describe the dynamics of molecular gas in the whole range of gas rarefaction. The model equation applied in this work is initially developed by Rykov [29] and recently extended to reflect the proper relaxations of energy and heat-flux exchanges between translational and internal modes [30]. Two velocity distribution functions (VDFs), $f_0(t,\boldsymbol{x},\boldsymbol{\xi})$ and $f_1(t,\boldsymbol{x},\boldsymbol{\xi})$, are used to describe the translational and internal states of gas molecules, where t is the time, $\boldsymbol{x}=(x_1,x_2,x_3)$ is the spatial coordinate, and $\boldsymbol{\xi}=(\xi_1,\xi_2,\xi_3)$ is the molecular velocity. We assume the internal degrees of freedom is d_r. The macroscopic quantities, such as the mass density ρ, flow velocity $\boldsymbol{u}$, deviatoric stress σ, translational and rotational temperature T_t and T_r, translational and rotational heat flux $\boldsymbol{q}_t$ and $\boldsymbol{q}_r$, are obtained by taking moments of VDFs f_0 and f_1:

$$\begin{aligned}
&\left(\rho,\, \rho\boldsymbol{u},\, \sigma,\, \frac{3}{2}\rho RT_t,\, \boldsymbol{q}_t\right) = \int \left(1,\, \boldsymbol{\xi},\, \boldsymbol{cc}-\frac{c^2}{3}\mathrm{I},\, \frac{c^2}{2},\, \frac{c^2}{2}\boldsymbol{c}\right) f_0 \mathrm{d}\boldsymbol{\xi}, \\
&\left(\frac{d_r}{2}\rho RT_r,\, \boldsymbol{q}_r\right) = \int (1,\, \boldsymbol{c}) f_1 \mathrm{d}\boldsymbol{\xi},
\end{aligned} \tag{3.1}$$

where $\boldsymbol{c}=\boldsymbol{\xi}-\boldsymbol{u}$ is the peculiar velocity and $\mathbf{I}$ is the 3×3 identity matrix. The total temperature T is defined as the equilibrium temperature between the translational and inter-

nal modes: $T=(3T_t+d_rT_r)/(3+d_r)$. The pressure related to the translational motion is $p_t=\rho RT_t$, while the total pressure is $p=\rho RT$, with $R=k_B/m$ being the gas constant.

In the absence of an external force, the evolution of VDFs is governed by the following kinetic equations:

$$\begin{aligned}\frac{\partial f_0}{\partial t}+\boldsymbol{\xi}\cdot\nabla f_0&=\frac{g_{0t}-f_0}{\tau}+\frac{g_{0r}-g_{0t}}{Z_r\tau},\\ \frac{\partial f_1}{\partial t}+\boldsymbol{\xi}\cdot\nabla f_1&=\frac{g_{1t}-f_1}{\tau}+\frac{g_{1r}-g_{1t}}{Z_r\tau},\end{aligned}\tag{3.2}$$

where terms in the left (right)-hand-side describe the streaming (collision); τ and $Z_r\tau$ are the elastic and inelastic collision characteristic time, respectively, with Z_r being the rotational collision number. The elastic collision conserves the kinetic energy, while the inelastic collision exchanges the translational and rotational energies. Here we choose $Z_r=10/3$ and the collision time is determined by

$$\tau=\frac{\mu}{p_t},\tag{3.3}$$

where μ is the shear viscosity. The power-law intermolecular potential is considered, so that the viscosity can be expressed as $\mu(T_t)=\mu(T_0)(T_t/T_0)^{\omega}$, with ω the viscosity index and T_0 the reference temperature. Here, we choose $\omega=0.74$.

The reference distribution functions are given by:

$$\begin{aligned}g_{0t}&=\rho\left(\frac{1}{2\pi RT_t}\right)^{3/2}\exp\left(-\frac{c^2}{2RT_t}\right)\left[1+\frac{2\boldsymbol{q}_t\cdot\boldsymbol{c}}{15RT_tp_t}\left(\frac{c^2}{2RT_t}-\frac{5}{2}\right)\right],\\ g_{0r}&=\rho\left(\frac{1}{2\pi RT}\right)^{3/2}\exp\left(-\frac{c^2}{2RT}\right)\left[1+\frac{2\boldsymbol{q}_0\cdot\boldsymbol{c}}{15RTp}\left(\frac{c^2}{2RT}-\frac{5}{2}\right)\right],\\ g_{1t}&=\frac{d_r}{2}RT_rg_{0t}+\left(\frac{1}{2\pi RT_t}\right)^{3/2}\frac{\boldsymbol{q}_r\cdot\boldsymbol{c}}{RT_t}\exp\left(-\frac{c^2}{2RT_t}\right),\\ g_{1r}&=\frac{d_r}{2}RTg_{0r}+\left(\frac{1}{2\pi RT}\right)^{3/2}\frac{\boldsymbol{q}_1\cdot\boldsymbol{c}}{RT}\exp\left(-\frac{c^2}{2RT}\right),\end{aligned}\tag{3.4}$$

with $\boldsymbol{q}_0$, $\boldsymbol{q}_1$ being linear combinations of translational and internal heat fluxes:

$$\begin{bmatrix}\boldsymbol{q}_0\\ \boldsymbol{q}_1\end{bmatrix}=\begin{bmatrix}(2-3A_{tt})Z_r+1 & -3A_{tr}Z_r\\ -A_{rt}Z_r & -A_{rr}Z_r+1\end{bmatrix}\begin{bmatrix}\boldsymbol{q}_t\\ \boldsymbol{q}_r\end{bmatrix},\tag{3.5}$$

where $\boldsymbol{A}=[A_{tt},A_{tr},A_{rt},A_{rr}]$ is determined by the relaxation rates of heat flux. In this paper, $A_{tt}=0.786, A_{tr}=-0.201, A_{rt}=-0.059$, and $A_{rr}=0.842$, as extracted from the DSMC [30]. Thus, in the continuum flow regime, the transitional and rotational thermal conductivities κ_t and κ_r can be derived from the kinetic model by the Chapman-Enskog expansion as [30]:

$$\begin{bmatrix}\kappa_t\\ \kappa_r\end{bmatrix}=\frac{\mu}{2}\begin{bmatrix}A_{tt} & A_{tr}\\ A_{rt} & A_{rr}\end{bmatrix}^{-1}\begin{bmatrix}5\\ d_r\end{bmatrix}.\tag{3.6}$$

Note that the collision terms in Eq. (3.2) becomes zero when the equilibrium state is reached, i.e., when the VDFs take the following form:

$$\begin{aligned} f_0^{eq}(\rho,\boldsymbol{u},T) &= \rho\left(\frac{1}{2\pi RT}\right)^{3/2}\exp\left(-\frac{c^2}{2RT}\right), \\ f_1^{eq}(\rho,\boldsymbol{u},T) &= \frac{d_r}{2}RTf_0^{eq}(\rho,\boldsymbol{u},T). \end{aligned} \tag{3.7}$$

3.2 The discretization of velocity space and quadrature

In DVM, the continuous velocity space $\boldsymbol{\xi}$ is discretized, where the way of discretization and the corresponding quadrature significantly affect the numerical accuracy and efficiency. Here, three types of velocity discretization are considered.

- The Newton-Cotes quadrature with uniform discretization of the truncated velocity space. Since after the normalization of the molecular velocity by $\sqrt{RT}$, the equilibrium VDF is close to $\exp(-\xi^2/2)$, the velocity space is truncated to the region of $[a,b]=[-5\sqrt{RT},5\sqrt{RT}]$, and the quadrature of the function g (e.g., the product of VDF and velocity moments) can be approximated as

$$\int_a^b g(\xi)d\xi \approx \sum_{i=1}^{N} g(\xi_i)\omega_i, \tag{3.8}$$

  where the integration point $\xi_i=a+h(i-1)$, with $h=(b-a)/(N-1)$ and $i=1,2,\cdots,N$; ω_i is the i-th weight, which can be set to h when the trapezoidal rule is applied. The cross product method can be applied when evaluating three-dimensional integration.

- The Gauss-Hermite quadrature.

$$\int_{-\infty}^{+\infty} g(\xi)d\xi = \int_{-\infty}^{+\infty}\exp(-\xi^2)\frac{g(\xi)}{\exp(-\xi^2)}d\xi \approx \sum_{i=1}^{N} g(\xi_i)\frac{\omega_i}{\exp(-\xi_i^2)}, \tag{3.9}$$

  where ξ_i and ω_i are the nodes and weights of the Gauss-Hermite quadrature. Since this quadrature has the highest algebraic accuracy, i.e., the integration error is zero when $g(\xi)\exp(\xi^2)$ is a polynomial of ξ with order less than or equal to $2N-1$, the Gauss-Hermite quadrature can effectively reduce the number of discretized velocity for low-speed near-equilibrium flows [31,32]. The cross product method can be applied when evaluating three-dimensional integration.

- When the cylindrical coordinates are used, the velocity points in the x-z plane are transformed from ξ_x and ξ_z to ξ_r and θ. In the ξ_r direction, the distribution function

is defined on $(0,+\infty)$, and we employ the Gauss-Laguerre quadrature:

$$\begin{aligned}\int_0^\infty g(\xi_r)\xi_r d\xi_r &= \int_0^\infty \frac{g(\xi_r)}{\exp(-\xi_r^2)}\xi_r \exp(-\xi_r^2)d\xi_r \\ &\overset{x=\xi_r^2}{=} \frac{1}{2}\int_0^\infty \frac{g(\sqrt{x})}{\exp(-x)}\exp(-x)dx \\ &\approx \sum_{i=1}^{N_r}\frac{1}{2}\frac{g(\sqrt{x_i})}{\exp(-x_i)}\omega_i = \sum_{i=1}^{N_r}\frac{1}{2}\frac{g(\xi_i)}{\exp(-\xi_i^2)}\omega_i,\end{aligned} \tag{3.10}$$

where x_i and ω_i are the nodes and weights in the Gauss-Laguerre quadrature, and $\xi_i=\sqrt{x_i}$. In the ξ_y direction, the Gauss-Hermite quadrature of order N_y is used, while in the θ direction, the Newton-Cotes quadrature is applied with N_θ uniform sections. Eventually, the integral in the cylindrical coordinates are:

$$\begin{aligned}\iiint_{\boldsymbol{\xi}} g d\boldsymbol{\xi} &= \int_0^{2\pi}\int_0^\infty\int_{-\infty}^\infty g(\xi_r,\theta,\xi_y)\xi_r d\xi_y d\xi_r d\theta \\ &\approx \frac{2\pi}{N_\theta}\sum_{j=1}^{N_\theta}\sum_{k=1}^{N_y}\frac{\omega_k}{\exp(-\xi_k^2)}\int_0^\infty g(\xi_r,\theta_j,\xi_k)\xi_r d\xi_r \\ &\approx \frac{\pi}{N_\theta}\sum_{i=1}^{N_r}\sum_{j=1}^{N_\theta}\sum_{k=1}^{N_y} g(\xi_i,\theta_j,\xi_k)\frac{\omega_k}{\exp(-\xi_k^2)}\frac{\omega_i}{\exp(-\xi_i^2)}.\end{aligned} \tag{3.11}$$

3.3 The wall boundary conditions

The Boltzmann kinetic equation describes the gas-gas interaction. To fully determine the rarefied gas flows, the gas-surface boundary condition should be specified. In the present paper, the diffuse, absorption and toroidal symmetry boundary conditions will be considered.

First, the diffuse boundary condition is applied at the wall, where gas molecules are reflected diffusely from the moving wall in thermodynamic equilibrium. The velocity distribution of gas molecules at the moving wall is given by:

$$f_{0,\text{wall}} = \begin{cases} f_{0,in}, & \boldsymbol{n}\cdot\boldsymbol{\xi}\geq 0, \\ f_0^{\text{eq}}(\rho_{\text{wall}},\mathbf{0},T_{\text{wall}}), & \boldsymbol{n}\cdot\boldsymbol{\xi}<0, \end{cases} \tag{3.12}$$

where $f_{0,\text{in}}$ is the VDF of gas molecules incident on the wall, T_{wall} is the wall temperature, and the density ρ_{wall} is determined by the non-penetration condition:

$$\int_{\boldsymbol{n}\cdot\boldsymbol{\xi}\geq 0}\boldsymbol{n}\cdot\boldsymbol{\xi} f_{0,\text{in}}\mathrm{d}\boldsymbol{\xi} = -\int_{\boldsymbol{n}\cdot\boldsymbol{\xi}<0}\boldsymbol{n}\cdot\boldsymbol{\xi} f_0^{\text{eq}}(\rho_{\text{wall}},\mathbf{0},T_{\text{wall}})\mathrm{d}\boldsymbol{\xi}. \tag{3.13}$$

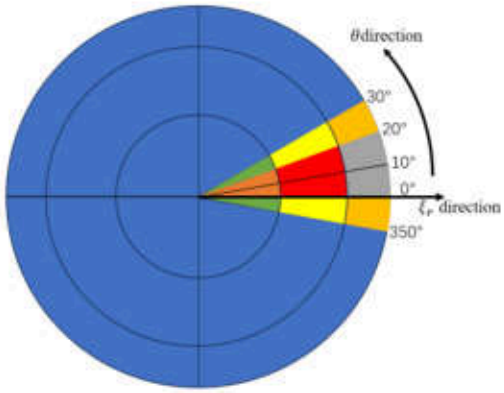

Figure 2: A schematic diagram of two-dimensional polar coordinate velocity discretization.

Similarly, the boundary condition for the internal degree of freedom is given by

$$f_{1,\text{wall}} = \begin{cases} f_{1,in}, & \boldsymbol{n}\cdot\boldsymbol{\xi} \geq 0, \\ \frac{d_r}{2} RT_{\text{wall}} f_0^{\text{eq}}(\rho_{\text{wall}}, \mathbf{0}, T_{\text{wall}}), & \boldsymbol{n}\cdot\boldsymbol{\xi} < 0. \end{cases} \tag{3.14}$$

Second, the absorption boundary condition is applied at the absorption pump, i.e., the blue area in Fig. 1(b,c).

$$\begin{aligned} f_{0,\text{pump}} &= \begin{cases} f_{0,in}, & \boldsymbol{n}\cdot\boldsymbol{\xi} \geq 0, \\ (1-\zeta) f_0^{\text{eq}}(\rho_{\text{wall}}, \mathbf{0}, T_{\text{wall}}), & \boldsymbol{n}\cdot\boldsymbol{\xi} < 0, \end{cases} \\ f_{1,\text{pump}} &= \begin{cases} f_{1,in}, & \boldsymbol{n}\cdot\boldsymbol{\xi} \geq 0, \\ (1-\zeta) \frac{d_r}{2} RT_{\text{wall}} f_0^{\text{eq}}(\rho_{\text{wall}}, \mathbf{0}, T_{\text{wall}}), & \boldsymbol{n}\cdot\boldsymbol{\xi} < 0. \end{cases} \end{aligned} \tag{3.15}$$

The implementation of the diffuse and absorption boundary conditions is elaborated in Ref. [33].

Third, the symmetry boundary condition is applied on the lateral walls in Fig. 1(b), with the help of cylindrical coordinates to avoid the interpolation in the velocity space. Since the 20° sector is simulated, we discretize the velocity space in the θ direction uniformly, with $\Delta\theta = 10°$, see Fig. 2. As shown in Figs. 1(b) and 1(c), the front lateral wall projected in the xz plane has the polar angle of $-10°$, hence the symmetry boundary condition reads

$$f(\xi_r, \theta, \xi_y) = f(\xi_r, -20° - \theta, \xi_y), \quad \theta \in [-10°, 170°], \tag{3.16}$$

while at the back lateral wall in Figs. 1(b) and 1(c), with the polar angle being 10° when projected to the xz plane, the boundary condition reads

$$f(\xi_r, \theta, \xi_y) = f(\xi_r, 20° - \theta, \xi_y), \quad \theta \in [-170°, 10°]. \tag{3.17}$$

3.4 The GSIS

After the velocity discretization, the kinetic equation can be solved by the iteration scheme in the finite volume framework [25]. Since the two kinetic equations in Eq. (3.2) have the same structure, to keep the presentation simple, we use the VDF f to stand for either f_0 or f_1. Also, as here we focus on the spatial discretization, the index for the velocity discretization does not appear in the VDF.

Given the VDF and the macroscopic quantities in the n-th iteration step, the VDF at the $(n+1)$-th step can be obtained as

$$\frac{f_i^{n+1}-f_i^n}{\Delta t}+\frac{1}{V_i}\sum_{j\in N(i)}\xi_n f_{ij}^{n+1}S_{ij}=\frac{g_i^n-f_i^{n+1}}{\tau_i^n}, \tag{3.18}$$

where

$$g=\left(1-\frac{1}{Z_r}\right)g_t+\frac{1}{Z_r}g_r. \tag{3.19}$$

Here, V_i is the volume of the i-th cell, S_{ij} is the area of this cell and the Δt is the time step.

This is the traditional DVM. Since the reference distribution function is evaluated at the n-th iteration step, it has large numerical dissipation at low spatial resolution. Therefore, in GSIS, the macroscopic synthetic equations are used to guide the evolution of the VDF. Firstly, by modifying Eq. (3.18), we obtain the VDF at the intermediate iteration step $n+1/2$:

$$\frac{f_i^{n+1/2}-f_i^n}{\Delta t}+\frac{1}{V_i}\sum_{j\in N(i)}\xi_n f_{ij}^{n+1/2}S_{ij}=\frac{g_i^n-f_i^{n+1/2}}{\tau_i^n}. \tag{3.20}$$

Secondly, we solve the following macroscopic synthetic equations to get the macroscopic quantities at the $(n+1)$-th iteration step:

$$\begin{aligned}
&\frac{\partial\rho}{\partial t}+\nabla\cdot(\rho\boldsymbol{u})=0,\\
&\frac{\partial}{\partial t}(\rho\boldsymbol{u})+\nabla\cdot(\rho\boldsymbol{u}\boldsymbol{u})+\nabla\cdot\boldsymbol{P}=0,\\
&\frac{\partial}{\partial t}(\rho e)+\nabla\cdot(\rho e\boldsymbol{u})+\nabla\cdot(\boldsymbol{P}\cdot\boldsymbol{u}+\boldsymbol{q}_t+\boldsymbol{q}_r)=0,\\
&\frac{\partial}{\partial t}(\rho e_r)+\nabla\cdot(\rho e_r\boldsymbol{u}+\boldsymbol{q}_r)=\frac{d_r\rho R}{2}\frac{T-T_r}{Z_r\tau}.
\end{aligned} \tag{3.21}$$

Here, $e_r=d_rRT_r/2$ and $e=(3RT_t+u^2)/2+e_r$ are the specific total and internal energies, respectively; the pressure tensor $\boldsymbol{P}$ is given by $\boldsymbol{P}=p_t\mathrm{I}+\sigma$. For general rarefied flows, the constitutive relation of the macroscopic equation should not only include Newton's law and Fourier's law of viscosity and heat flux, but also consider the higher-order rarefied

effect:

$$\begin{aligned}
\boldsymbol{\sigma}^{n+1} &= \boldsymbol{\sigma}_{\mathrm{NSF}}^{n+1} + \underbrace{\int \left(\boldsymbol{c}\boldsymbol{c} - \frac{c^2}{3}\mathrm{I} \right) f_0^{n+1/2} \mathrm{d}\boldsymbol{v} - \boldsymbol{\sigma}_{\mathrm{NSF}}^{n+1/2}}_{\mathrm{HoT}_{\sigma}}, \\
\boldsymbol{q}_t^{n+1} &= \boldsymbol{q}_{t,\mathrm{NSF}}^{n+1} + \underbrace{\frac{1}{2}\int \boldsymbol{c}c^2 f_0^{n+1/2} \mathrm{d}\boldsymbol{v} - \boldsymbol{q}_{t,\mathrm{NSF}}^{n+1/2}}_{\mathrm{HoT}_{q_t}}, \\
\boldsymbol{q}_r^{n+1} &= \boldsymbol{q}_{r,\mathrm{NSF}}^{n+1} + \underbrace{\int \boldsymbol{c} f_1^{n+1/2} \mathrm{d}\boldsymbol{v} - \boldsymbol{q}_{r,\mathrm{NSF}}^{n+1/2}}_{\mathrm{HoT}_{q_r}},
\end{aligned} \tag{3.22}$$

where the Navier-Stokes constitutive relations are given as:

$$\begin{aligned}
\boldsymbol{\sigma}_{\mathrm{NSF}} &= -\mu \left(\nabla \boldsymbol{u} + \nabla \boldsymbol{u}^{\mathrm{T}} - \frac{2}{3} \nabla \cdot \boldsymbol{u} \mathrm{I} \right), \\
\boldsymbol{q}_{t,\mathrm{NSF}} &= -\kappa_t \nabla T_t, \\
\boldsymbol{q}_{r,\mathrm{NSF}} &= -\kappa_r \nabla T_r.
\end{aligned} \tag{3.23}$$

Thirdly, the VDF at the (n+1)-th step is given by:

$$\begin{aligned}
f_0^{n+1} &= f_0^{n+1/2} - f_0^{eq}(\boldsymbol{W}^{n+\frac{1}{2}}) + f_0^{eq}(\boldsymbol{W}^{n+1}), \\
f_1^{n+1} &= f_1^{n+1/2} - \frac{d_r}{2} R T_r^{n+1/2} f_0^{eq}(\boldsymbol{W}^{n+\frac{1}{2}}) + \frac{d_r}{2} R T_r^{n+1} f_0^{eq}(\boldsymbol{W}^{n+1}),
\end{aligned} \tag{3.24}$$

where $\boldsymbol{W} = \{\rho, \boldsymbol{u}, T_t\}$. The detailed implementation of the GSIS method can be found in our recent paper [25].

4 Convergence test and numerical efficiency

Convergence tests in both spatial and velocity spaces are carried out in GSIS. The simulation parameters are adopted from Ref. [1]: the number densities at the inner and outer entry gaps are 1×10^{21} m^{-3} and 1.857×10^{21} m^{-3}, respectively. The gas temperature is maintained at 293 K. Using a reference length of 1 dm, the Knudsen number

$$\mathrm{Kn} = \frac{\lambda}{L} \equiv \frac{\mu(T_0)}{p_0 L} \sqrt{\frac{\pi R T_0}{2}} \tag{4.1}$$

is 0.0426. Larger Knudsen number can be obtained by proportionally reducing the two number densities at the inner and outer entry gaps. The absorptivity is $\zeta = 0.3$.

Due to the complexity of the divertor's structure, a combination of structured and unstructured grid cells is employed, with 95% of the grid cells being hexahedral. At the junctions of these hexahedral grid cells, some tetrahedral grid cells are used. There are

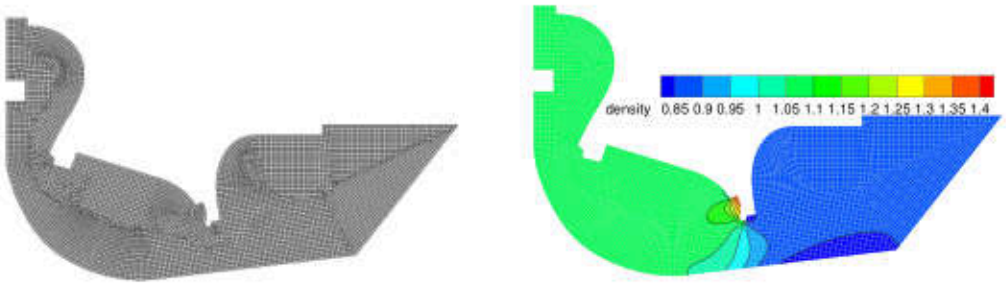

(a) (b)

Figure 3: (a) The projected mesh in the middle section at $z=0$. (b) The mesh independence test under the Cartesian coordinate system and Kn=0.0426. The background cloud is the normalized density by using 360,000 grid cells, while the black line is using 240,000.

6,268 grid cells in the middle section, with each grid having an area of approximately 1 cm^2, see Fig. 3(a). We run the numerical simulations with 240,000 and 360,000 physical mesh elements, and find that the two results overlap, see Fig. 3(b). This means the grid convergence is achieved and subsequent calculations employ 240,000 physical mesh elements.

We test the velocity mesh independence in the Cartesian coordinates, where the lateral walls in Fig. 1(b) are assumed to be solid walls with the diffuse gas-surface interaction. Firstly, we use the Newton-Cotes quadrature with $40\times40\times40$ discrete velocity points and $30\times30\times30$ discrete velocity points, and find both results overlap. These solutions are used as reference, see the black lines in Fig. 4(a). Then, we gradually replace the Newton-Cotes quadrature by the Gauss-Hermite quadrature, with reduced number of discretized velocities. Eventually we find that applying 10-point Gauss-Hermite quadrature in each velocity direction is adequate the capture the flow field, see red lines with points in Fig. 4(a). The computer resources are summarized in Table 1. It is seen that, i) the GSIS can find the steady-state solution within 100 iterations, ii) the simulation time (core hours=CPU cores $\times$ wall-clock time) can be reduced by about two orders of magnitude when the Gauss-Hermite quadrature is applied, and iii) the simulation time with GSIS is 20 times less than the DVM when using Newton-Cotes quadrature and the Gauss-Hermite quadrature.

We also test the velocity mesh independence in the cylindrical coordinates, where the lateral walls follow the symmetry boundary condition. When Kn$=0.0426$, we employ 36-point Newton-Cotes quadrature in the θ direction and 10-point Gauss-Hermite quadrature in ξ_y. We also apply the 40-point Newton-Cotes quadrature in the ξ_r direction to obtain a reference solution, see the black lines in Fig. 4(b). Then, we replace the Newton-Cotes quadrature by the Gauss-Laguerre quadrature in the ξ_r direction, and find that 18-point Gauss-Laguerre quadrature in ξ_r yields results (red dotted lines) identical

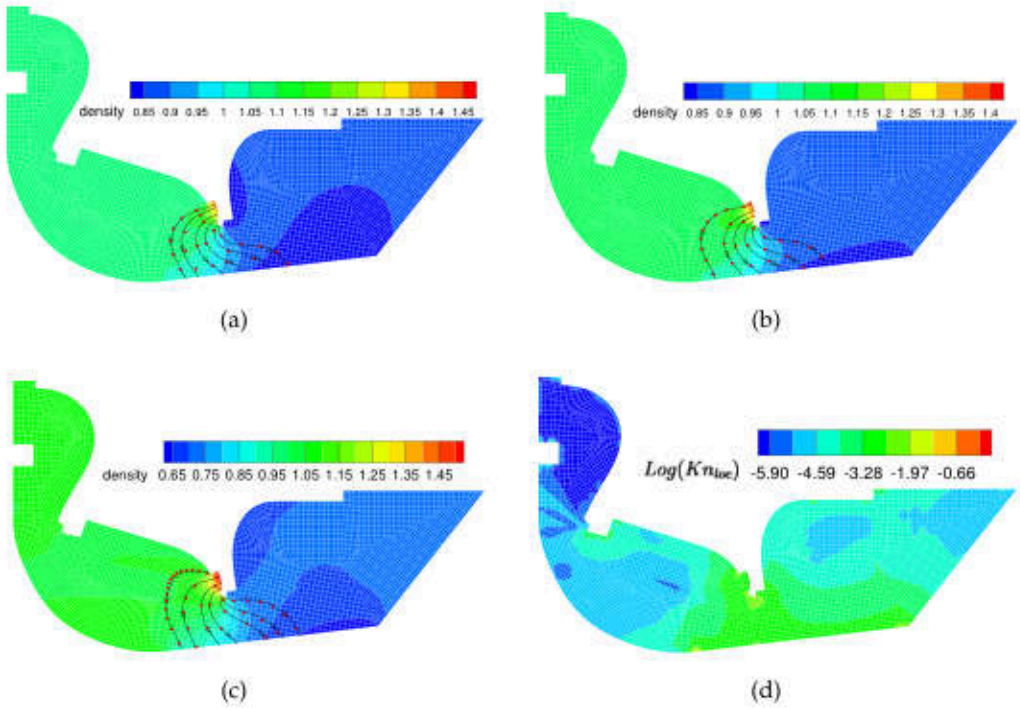

Figure 4: (a) Velocity mesh independence test under the Cartesian coordinate system and Kn$=0.0426$, when the lateral walls are diffuse. The black lines refer to the streamlines when the discrete velocity points are $30\times30\times30$, and the red dotted lines are the streamlines when the discrete velocity points are $10\times10\times10$ when using Gauss-Hermite quadrature. (b) and (c) Velocity mesh independence test under the cylindrical coordinate system, when the lateral walls follow the symmetry boundary condition and Kn$=0.0426$ and 4.26, respectively. The black lines refer to streamlines when the discrete velocity points are $36\times10\times40$, which uniformly disperse in polar coordinate for x-z plane and Gauss-Hermite quadrature for y-direction. The red dotted lines represent the streamlines after transforming the uniform dispersion in the z-direction in the velocity space dispersion mode of the black line into the Gauss-Laguerre quadrature dispersion. (d) The local Knudsen numbers when the absorptivity is $\zeta=0.8$ and the temperature is 300 K.

to the reference solution. When Kn=4.26, we establish a reference solution using 20-point Gauss-Hermite quadrature in ξ_y and 36-point Gauss-Laguerre quadrature in ξ_r, see the black lines in Fig. 4(c). We observe that identical results (red dotted lines) can also be obtained when using $36\times10\times18$ discrete velocity points. In the numerical simulation, the GSIS needs 128 cores, 88 iteration steps, and total 44 core hours to find the solution.

Compared with the DSMC simulation [1], where 40 million spatial cells and 0.688 million CPU core hours are used, the GSIS can be faster by about 4 orders of magnitude†.

†Note that we employ the cylindrical coordinates to precisely implement the symmetry boundary conditions at the two lateral walls, which is less efficient compared to Cartesian coordinates. For example, if the full divertor geometry (360°) were simulated using Cartesian coordinates instead of the 20° section shown in Fig. 1, with the $10\times10\times10$ Gauss-Hermite quadrature, the core hours required would be $4\times18=72$. In contrast, the DSMC method would require 18×0.688 million core hours, which is slower by five orders of magnitude. Simulating the full-scale divertor is advantageous, however, since in reality, perfect toroidal symmetry is not always achieved.

Table 1: Tests of velocity mesh independence in the Cartesian coordinates. NC30×GH30×GH10 means that the Newton-Cotes quadrature with 30 uniform grids are used in the ξ_x direction, 30 Gauss-Hermite nodes are used in the ξ_y direction, and 10 Gauss-Hermite nodes are used in the ξ_z direction. The Knudsen number is 0.0426, and the convergence criterion is the relative difference in density and temperature between two consecutive iterations is less than 10^{-5}.

discrete velocity	CPU cores	times (s)	iteration step	core hours
NC40×NC40×NC40 (DVM)	960	26593	1133	7091
NC40×NC40×NC40	640	1996	94	354
NC30×NC30×NC30	640	1308	92	232
NC30×NC30×GH10	320	695	92	61
NC30×GH10×GH10	256	199	98	14
GH10×GH10×GH10 (DVM)	128	4067	1897	144
GH10×GH10×GH10	128	118	64	4

This huge reduction of computational time is due to i) the asymptotic-preserving property of the GSIS, which allows use of coarse spatial grids, ii) the fast convergence property of the GSIS, which finds the steady state solution within 100 iterations, and iii) the deterministic nature of the GSIS, which does not suffer from the statistical error. It should be noted that the magnetic coils and the cooling pipes are not considered in the simplified geometry in Figs. 1(b) and 1(c). Even if they are added, the number of the spatial grids in GSIS would at most increase by 10 times, and the GSIS can still be faster than the DSMC by 3 orders of magnitude.

5 Roles of Knudsen numbers, absorptivity and temperature

In this section, we employ the GSIS with the cylindrical coordinates in the molecular velocity space to study the flow fields within the divertor and analyze the pumping speed under various absorptivity, temperature, and Knudsen numbers. All results are normalized using the following parameters:

$$T_{ref}=T_0,\quad v_{ref}=\sqrt{\frac{2k_BT_0}{m}},\quad p_{ref}=\rho_0RT_0. \tag{5.1}$$

The local Knudsen number is defined in terms of the local density gradient as:

$$\mathrm{Kn}_{GII}=\frac{l}{\rho/\nabla\rho}, \tag{5.2}$$

where l is the local mean free path. Fig. 4(d) show the local Knudsen number in logarithmic form when the gas temperature is 300 K and the absorptivity is 0.3. It is seen that the local Knudsen number spans approximately 4 orders of magnitude, from continuous flow to transition flow. Due to the limitations of the grid and time step size, the computational cost of the DSMC method will be greatly increased in continuum-flow problems.

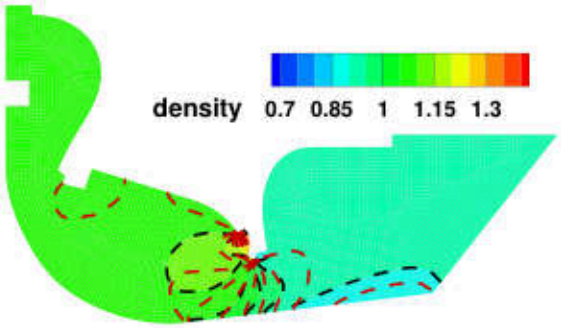

Figure 5: The normalized density distributions at the midsection ($z=0$) when Kn=4.26. The cloud image and black dotted lines are calculated using NS, while the red dotted lines are calculated using GSIS.

At the same time, from Fig. 5, it is seen that when the Knudsen number is 4.26, there is a significant difference between the density distribution of the middle section calculated by NS and GSIS, which means that the NS equations are no longer applicable in rarefied flows.

5.1 Role of Knudsen number and absorptivity

We first consider the case where the temperature of the inlet gas and the surface temperature is $T_0=300$ K. The coordinate systems in all results are shown in Figs. 1(b) and 1(c). Fig. 6 shows the pressure distribution in the midsection ($z=0$) of the divertor at varying Knudsen numbers and absorptivities. Because the flow velocity is much smaller than the sound speed, the gas flow exhibits minimal temperature fluctuations inside the divertor. Hence, the pressure can be deemed directly proportional to density. As the Knudsen number rises, the pressure variation within the divertor gradually increases, rendering the flow characteristics more intricate. As the absorptivity rises, both the pressure variation and the extent of the low-pressure zone increase. Fig. 7 illustrates the pressure distribution at the outlet pump, which is seen in Figs. 1(b) and 1(c). With the increase of Knudsen number, the pressure difference increases, and the pressure distribution becomes more complex. As the absorptivity increases, the pressure decreases, which means more gas escapes from the outlet pump.

The reduced density and pressure at the pump opening imply higher mass flow rate at higher absorptivity. Figs. 8(a) to 8(c) show the velocity distribution in the y-direction, across the divertor cross-section ($z=0$). The outlet pump is located within the range of $1850\leq x\leq 2250$. In this region, as x increases, the gas speed first increases and reaches its maximum near $x=2000$, then it decreases and reaches its minimum value around $x=2150$. Finally it gradually increases. The Knudsen number has small impact on the magnitude of the flow velocity, however, increasing the absorptivity will significantly enhance the velocity, thereby increasing the mass flow rate of the pump.

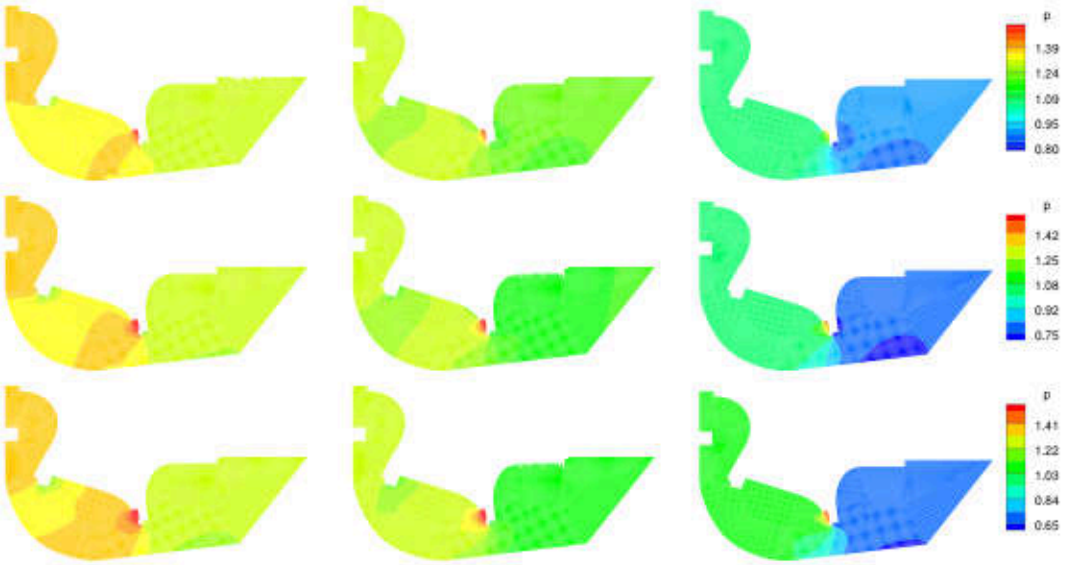

Figure 6: normalized pressure distributions at the midsection ($z=0$). The absorptivity from the left column to right column is 0.05, 0.1, 0.3, respectively. The Knudsen number from the top row to bottom row is 0.0426, 0.426, 4.26, respectively.

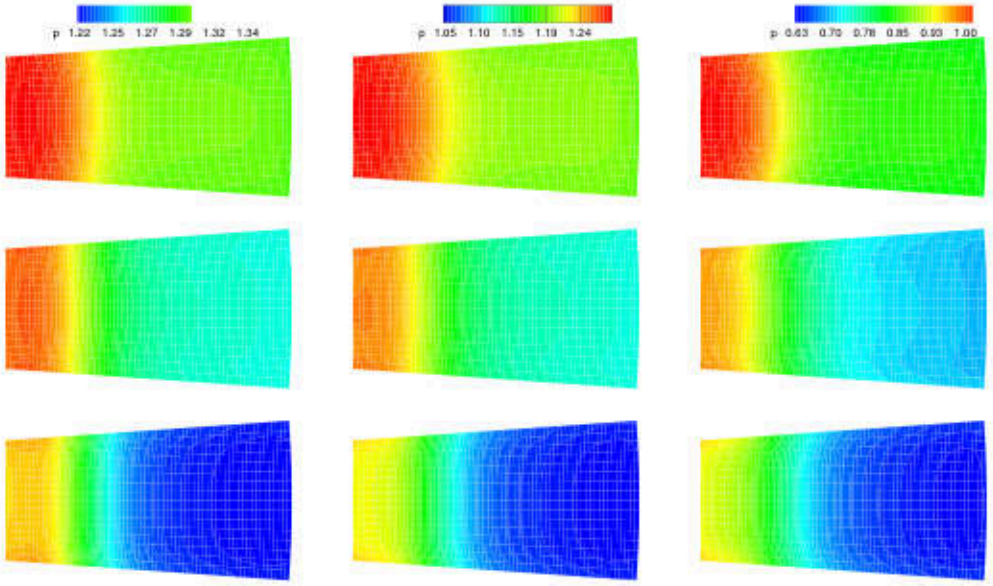

Figure 7: normalized pressure distributions at the absorption pump, which is located in the middle of the bottom of the divertor, see the blue area in Figs. 1(b) and 1(c). The absorptivity from the left column to right column is 0.05, 0.1, 0.3, respectively. The Knudsen number from the top row to bottom row is 0.00426, 0.0426, 0.426, respectively.

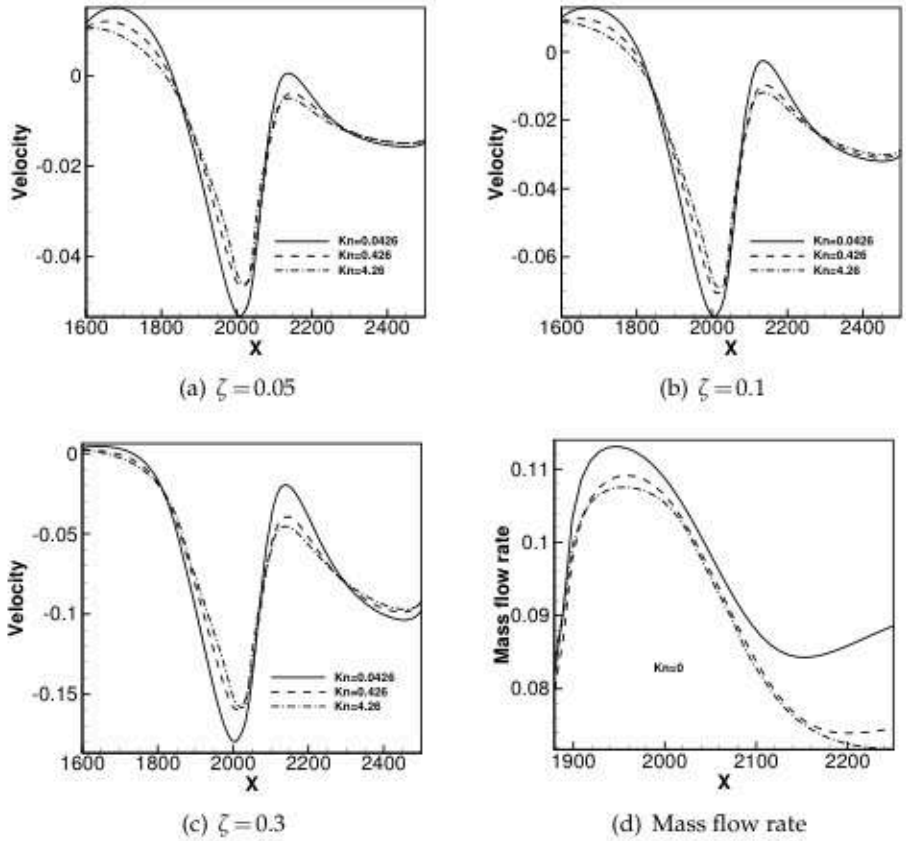

(a) $\zeta=0.05$ (b) $\zeta=0.1$

(c) $\zeta=0.3$ (d) Mass flow rate

Figure 8: (a-c) The normalized velocity in the y-direction of midsection ($z=0$). (d) The normalized mass flow distribution along the central axis ($z=0$) of the absorption pump for different Knudsen numbers (absorptivity= 0.3). Both the gas temperature at the inlet and the wall temperature are 300 K.

Fig. 8(d) shows the distribution of mass flow rate $\rho \boldsymbol{u}\cdot\boldsymbol{n}$ along the central axis of the absorption pump, assuming a constant absorptivity of 0.3, where $\boldsymbol{n}$ represents the outward normal vector at the pump opening. The maximum mass flow rate occurs at approximately $x_m=1950$, which is slightly to the left of the location where the speed is at its peak. For $x<x_m$, the mass flow rate increases monotonically with x. Conversely, for $x>x_m$, a monotonic decrease in the mass flow rate is observed only at large Knudsen numbers, such as Kn=4.26. At smaller Knudsen numbers, such as Kn=0.426 and 0.0426, a local minimum in the mass flow rate is present, that is, when x increases, the mass flow rate first decreases and then increases.

5.2 Role of inlet temperature

We now raise the gas temperature to $T_0=1000$ K, while keep the wall temperature at 300 K. Fig. 9 depicts the spatial distribution of temperature and pressure. Significant

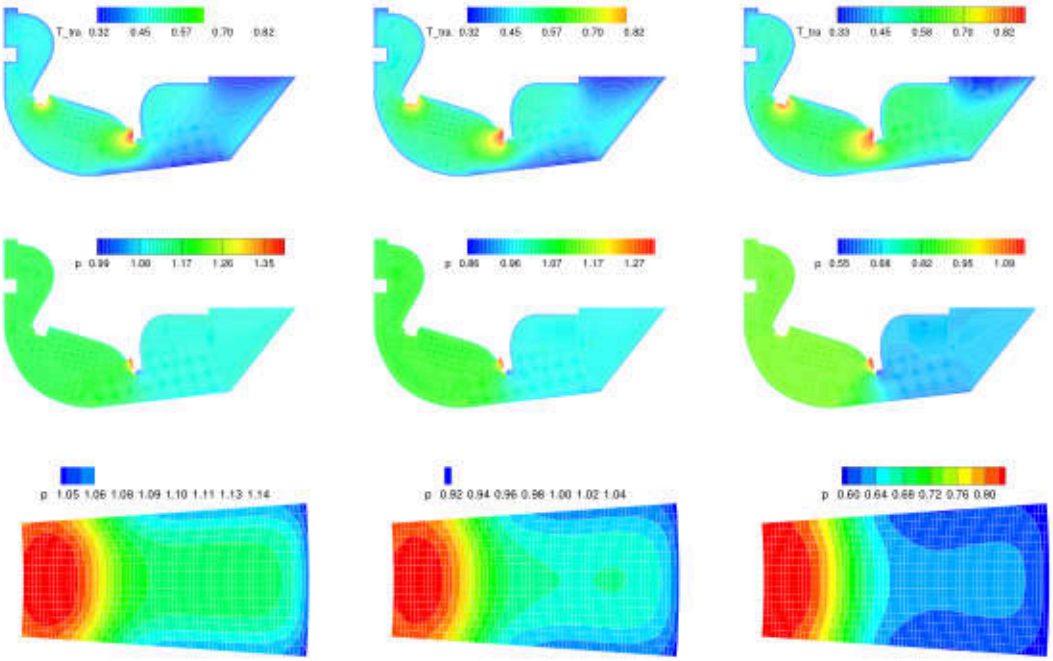

Figure 9: The normalized temperature and pressure distributions at the midsection ($z=0$) and pump opening under different absorptivity when Kn $=$ 0.054. The inlet gas temperature is 1000 K, while the wall temperature is 300 K.

temperature differences are observed near both the inner entry gap and the outer entry gap, highlighting the complex thermodynamic phenomena within the system and the evolution of temperature gradients across different regions. Fig. 9 also shows the pressure distribution at the outlet pump. The pressure profile manifests itself in a strip-like configuration that stretches from left to right, with a noticeable disparity observed between approximately one third of the area on the left side compared to the right side. Notably, a higher gas density emanates from the left side of the outlet pump, indicating a nonuniform distribution of pressure across the outlet.

Fig. 10(a-c) shows the velocity profile u_y in the middle section ($z=0$). Compared to Figs. 8(a) to 8(c), the speed also reaches its maximum velocity around $x=2000$, and the velocity increases with increasing gas temperature. Also, the velocity becomes much more sensitive to the Knudsen number. Fig. 10(d) shows the mass flow rate along the central axis ($z=0$) of the absorption pump for different Knudsen numbers. The peak mass flow rate appears around $x=1940$, rather than at $x=2000$ where the gas speed is maximum. This is because the gas density at the pumping opening drops significantly as x increases; see the third row in Fig. 9. Compared to Fig. 8(d), the mass flow rate varies significantly with the Knudsen number, indicating the significant impact of gas temperature on mass flow rate.

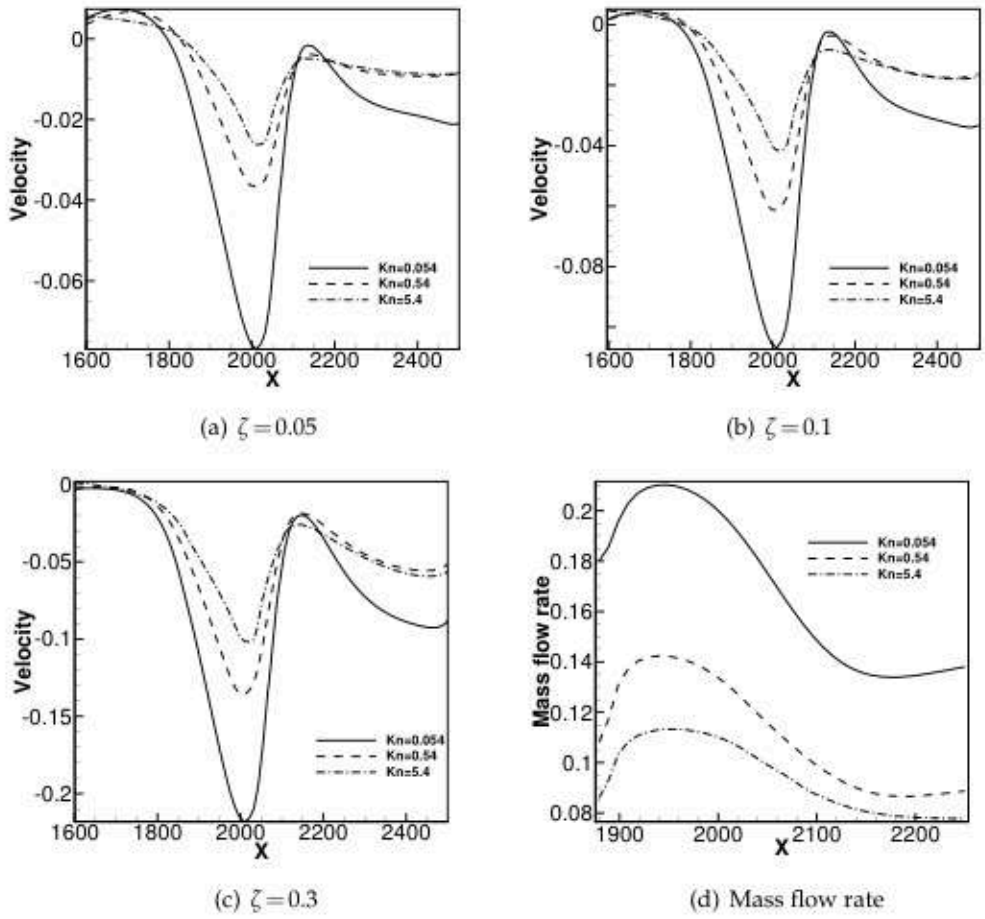

(a) $\zeta=0.05$ (b) $\zeta=0.1$

(c) $\zeta=0.3$ (d) Mass flow rate

Figure 10: (a-c) The normalized velocity in the y-direction of axial section. (d) The normalized mass flow distribution along the central axis ($z=0$) of the absorption pump with absorptivity=0.3. The inlet gas temperature is 1000 K, while the wall temperature is 300 K.

5.3 The pumping speed

The pumping speed is an important parameter in the design of divertor, which is defined as the mass flow rate over the average gas density:

$$S_p(\zeta)=\frac{\text{mass flow rate}}{\text{average density}}=\frac{\int_S \rho \boldsymbol{u}\cdot\boldsymbol{n}dS}{(\int_S \rho dS)/S'} \tag{5.3}$$

where $\boldsymbol{v}$ is the velocity of the gas, S is the area of the pump, and $\boldsymbol{n}$ is the outward normal vector of the pump surface.

In Fig. 11(a), a direct correlation is observed between the mass flow rate through the absorption pump and the Knudsen number at various absorptivity. The results indicate

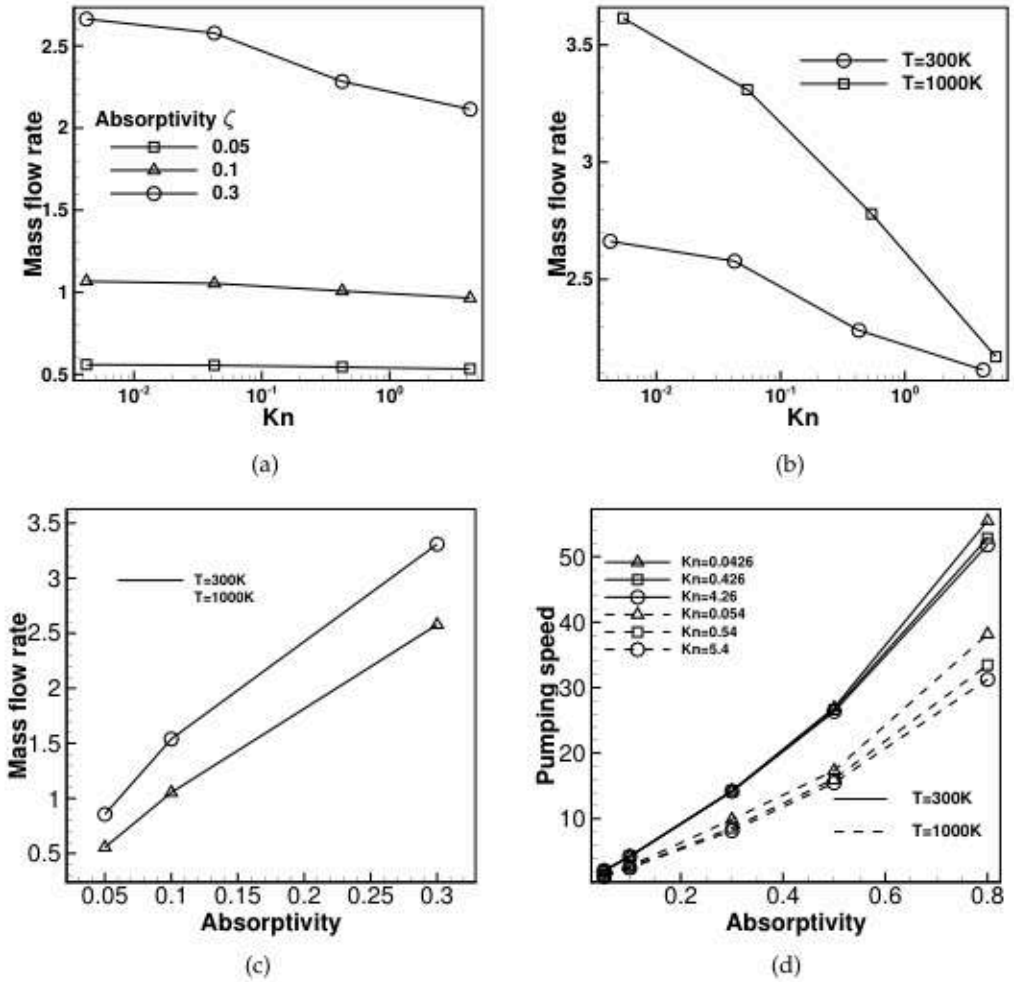

Figure 11: (a) The normalized mass flow under different absorptivity and Knudsen number when gas temperature is 300 K. (b) The normalized mass flow under different temperature and Knudsen number when the absorptivity is 0.3. (c) The normalized mass flow under different absorptivity and temperature when Kn=0.0426. (d) Pumping speed under different absorptivity and Knudsen number.

that as the Knudsen number increases, the gas within the divertor tends to become rarefied, leading to a gradual decrease in the mass flow rate through the absorption pump. This trend is further accentuated with higher absorptivity. However, the pumping rate shows minimal variation with changes in the Knudsen number when absorptivity is small. This suggests that the efficiency of the absorption pump is significantly influenced by the rarefaction of the gas within the deflector, particularly under the conditions of increased Knudsen numbers and absorptivity. The findings underscore the importance of considering the Knudsen number and absorptivity in optimizing the performance of absorption pumps in rarefied gas flow environments.

Fig. 11(b) shows that when the absorption rate is 0.3, the mass flow rate changes with Knudsen number at different temperatures. It can be seen that at low Knudsen number, increasing temperature significantly improves the mass flow rate of the pump, and this effect gradually decreases when the Knudsen number increase.

Fig. 11(c) shows the mass flow through the absorption pump under different absorptivity and temperature. With an increase in absorptivity, the mass flow rate shows a trend of logarithmic increase, and the increase of the temperature significantly increased the mass flow rate through the absorption pump.

Fig. 11(d) shows the correlation between pumping speed and absorptivity at various Knudsen numbers. It is seen that for higher absorptivity, there is a slight reduction in velocity with an increase in the Knudsen number. At elevated temperatures, the mass flow rate through the absorption pump increases, while the pumping speed decreases. This indicates that the impact of temperature elevation on density distribution is more pronounced.

6 Conclusions

We have simulated a simplified version of the latest three-dimensional divertor using a general synthetic iterative scheme, with the velocity space discretized in cylindrical coordinates. Due to its asymptotic-preserving nature and rapid convergence, and given that the gas flow inside the divertor is much lower than the sound speed, the simulation efficiency of GSIS is significantly higher than that of the traditional DSMC method. Using this efficient numerical method, we have analyzed the flow fields inside the divertor across a wide range of Knudsen numbers, absorptivity levels, and gas temperatures. The simulation results indicate that higher absorption rates lead to a substantial increase in mass flow rate and pumping speed through the absorption pump. Additionally, increasing the gas temperature also significantly enhances the mass flow rate. The numerical method and findings provide valuable tools and insights into the performance of the new Tokamak model under various conditions, supporting the ongoing development of nuclear fusion technology.

Acknowledgments

This work is supported by the "Climbing Program" for scientific and Technological Innovation in Guangdong (pdjh2024c10701).

References

[1] C. Tantos, S. Varoutis, V. Hauer, C. Day, P. Innocente, 3D numerical study of neutral gas dynamics in the DTT particle exhaust using the DSMC method, Nucl. Fusion 64 (1) (2023) 016019.

[2] S. Varoutis, C. Gleason-González, D. Moulton, U. Kruezi, M. Groth, C. Day, S. Wiesen, D. Harting, JET EFDA Contributors, Simulation of neutral gas flow in the jet sub-divertor, Fusion Engineering and Design 121 (2017) 13–21.
[3] C. Gleason-González, S. Varoutis, X. Luo, K. Shimizu, T. Nakano, K. Hoshino, H. Kawashima, N. Asakura, C. Day, S. Sakurai, Simulation of collisional effects on divertor pumping in JT-60SA, Fusion Engineering and Design 109 (2016) 693–699.
[4] L. Affinito, A. Anemona, M. Apicella, P. Batistoni, G. Calabrò, A. Cardinali, S. Ceccuzzi, C. Centioli, V. Corato, P. Costa, et al., DTT: Divertor Tokamak Test facility Project Proposal, ENEA, 2015.
[5] L. Affinito, S. Almaviva, A. Anemona, M. Angelone, M. Apicella, A. Appi, G. Apruzzese, G. Artaserse, G. Barone, M. Baruzzo, et al., DTT Divertor Tokamak Test facility–Interim Design Report, ENEA Italian National Agency for New Technologies, 2019.
[6] G. A. Bird, Molecular Gas Dynamics and the Direct Simulation of Gas Flows, Oxford Science Publications, Oxford University Press Inc, New York, 1994.
[7] V. Aristov, Direct Methods for Solving the Boltzmann Equation and Study of Nonequilibrium Flows, Springer, 2001.
[8] T. E. Schwartzentruber, I. D. Boyd, A hybrid particle-continuum method applied to shock waves, Journal of Computational Physics 215 (2) (2006) 402–416.
[9] T. E. Schwartzentruber, L. C. Scalabrin, I. D. Boyd, A modular particle–continuum numerical method for hypersonic non-equilibrium gas flows, Journal of Computational Physics 225 (1) (2007) 1159–1174.
[10] L. Pareschi, G. Russo, Time relaxed Monte Carlo methods for the Boltzmann equation, SIAM Journal on Scientific Computing 23 (4) (2001) 1253–1273.
[11] E. Gabetta, L. Pareschi, G. Toscani, Relaxation schemes for nonlinear kinetic equations, SIAM Journal on Numerical Analysis 34 (6) (1997) 2168–2194.
[12] G. Dimarco, L. Pareschi, Exponential Runge–Kutta methods for stiff kinetic equations, SIAM Journal on Numerical Analysis 49 (5) (2011) 2057–2077.
[13] W. Ren, H. Liu, S. Jin, An asymptotic-preserving Monte Carlo method for the Boltzmann equation, Journal of Computational Physics 276 (2014) 380–404.
[14] F. Fei, J. Zhang, J. Li, Z. Liu, A unified stochastic particle Bhatnagar-Gross-Krook method for multiscale gas flows, Journal of Computational Physics 400 (2020) 108972.
[15] M. Pfeiffer, F. Garmirian, M. H. Gorji, Exponential Bhatnagar-Gross-Krook integrator for multiscale particle-based kinetic simulations, Physical Review E 106 (2) (2022) 025303.
[16] S. Kim, W. Park, E. Jun, A second-order particle Fokker-Planck model for rarefied gas flows, Computer Physics Communications 304 (2024) 109323.
[17] J. Yang, J. Huang, Rarefied flow computations using nonlinear model Boltzmann equations, Journal of Computational Physics 120 (2) (1995) 323–339.
[18] K. Aoki, P. Degond, L. Mieussens, et al., Numerical simulations of rarefied gases in curved channels: Thermal creep, circulating flow, and pumping effect, Communications in Computational Physics 6 (5) (2009) 919.
[19] Y. J. Zhu, C. W. Zhong, K. Xu, Implicit unified gas-kinetic scheme for steady state solutions in all flow regimes, J. Comput. Phys. 315 (2016) 16–38.
[20] Z. L. Guo, K. Xu, R. J. Wang, Discrete unified gas kinetic scheme for all Knudsen number flows: Low-speed isothermal case, Phys. Rev. E 88 (2013) 033305.
[21] W. Su, L. H. Zhu, P. Wang, Y. H. Zhang, L. Wu, Can we find steady-state solutions to multiscale rarefied gas flows within dozens of iterations?, J. Comput. Phys. 407 (2020) 109245.
[22] W. Su, Y. H. Zhang, L. Wu, Multiscale simulation of molecular gas flows by the general

synthetic iterative scheme, Comput. Methods Appl. Mech. Engrg. 373 (2021) 113548.
[23] J. N. Zeng, R. F. Yuan, Y. Zhang, Q. Li, L. Wu, General synthetic iterative scheme for polyatomic rarefied gas flows, Computers and Fluids 265 (2023) 105998.
[24] Y. J. Zhu, C. W. Zhong, K. Xu, An implicit unified gas-kinetic scheme for unsteady state solutions in all flow regimes, J. Comput. Phys. 386 (2019) 190–217.
[25] Y. Zhang, J. Zeng, R. Yuan, W. Liu, Q. Li, L. Wu, Efficient parallel solver for rarefied gas flow using GSIS, Comput. Fluids 281 (2024) 106374.
[26] C. Tantos, S. Varoutis, C. Day, Deterministic and stochastic modeling of rarefied gas flows in fusion particle exhaust systems, Journal of Vacuum Science & Technology B 38 (6) (2020).
[27] S. Varoutis, Y. Igitkhanov, C. Day, Assessment of the 3D geometrical effects on the DEMO divertor pumping efficiency, Nucl. Mater. Energy 19 (2019) 120–123.
[28] C. S. Wang-Chang, G. E. Uhlenbeck, Transport Phenomena in Polyatomic Gases, University of Michigan Engineering Research Rept. No. CM-681, 1951.
[29] V. A. Rykov, V. N. Skobelkin, Macroscopic description of the motions of a gas with rotational degrees of freedom, Fluid Dyn. 13 (1978) 144.
[30] Q. Li, J. N. Zeng, W. Su, L. Wu, Uncertainty quantification in rarefied dynamics of molecular gas: rate effect of thermal relaxation, J. Fluid Mech. 917 (2021) A58.
[31] V. E. Ambruş, V. Sofonea, High-order thermal lattice Boltzmann models derived by means of Gauss quadrature in the spherical coordinate system, Phys. Rev. E 86 (2012) 016708.
[32] Y. Y. Shi, L. Wu, X. W. Shan, Accuracy of high-order lattice Boltzmann method for non-equilibrium gas flow, J. Fluid Mech. 907 (2021) A25.
[33] W. Liu, Y. B. Zhang, J. N. Zeng, L. Wu, Further acceleration of multiscale simulation of rarefied gas flow via a generalized boundary treatment, J. Computat. Phys. 503 (2024) 112830.